Steel and Composite Structures, *Vol. 22*, *No. 1* (*2016*) *161-182*
DOI: http://dx.doi.org/10.12989/scs.2016.22.1.161

A state space meshless method for the 3D analysis of FGM axisymmetric circular plates

Chih-Ping Wu* and Yan-Cheng Liu

Department of Civil Engineering, National Cheng Kung University, 1 University Road, Tainan 70101, Taiwan, Republic of China

(*Received June 03, 2016, Revised September 21, 2016, Accepted September 25, 2016*)

Abstract. A state space differential reproducing kernel (DRK) method is developed for the three-dimensional (3D) analysis of functionally graded material (FGM) axisymmetric circular plates with simply-supported and clamped edges. The strong formulation of this 3D elasticity axisymmetric problem is derived on the basis of the Reissner mixed variational theorem (RMVT), which consists of the Euler-Lagrange equations of this problem and its associated boundary conditions. The primary field variables are naturally independent of the circumferential coordinate, then interpolated in the radial coordinate using the early proposed DRK interpolation functions, and finally the state space equations of this problem are obtained, which represent a system of ordinary differential equations in the thickness coordinate. The state space DRK solutions can then be obtained by means of the transfer matrix method. The accuracy and convergence of this method are examined by comparing their solutions with the accurate ones available in the literature.

Keywords: circular plates; functionally graded material; meshless methods; reproducing kernels; state space methods; three-dimensional analysis

1. Introduction

In recent years a new class of advanced composites, functionally graded materials (FGMs), has been produced by mixing two or more constituent phases with continuous and smoothly varying composition. FGMs possess a number of benefits, such as reduction of stress concentration at interfaces between adjacent layers, enhanced thermal properties and higher fracture toughness (Birman and Byrd 2007, Dai *et al*. 2016, Jha *et al*. 2013). FGMs are thus widely used as advanced structural materials in many engineering applications, such as dental and orthopedic implants (Watari *et al*. 1997), nuclear fusion reactors (Koizumi 1997), sensors and thermogenerators (Müller *et al*. 2003) and wear resistant coatings (Schulz *et al*. 2003). Because the material properties of FGM structures can be designed as inhomogeneous, and thus vary continuously and smoothly through the thickness coordinate of these, they have better performance than laminated composite ones, the material properties of which are layerwise constant distributions through the thickness coordinate, and change suddenly at the interfaces between adjacent layers. The

*Corresponding author, Professor, E-mail: cpwu@mail.ncku.edu.tw

Copyright © 2016 Techno-Press, Ltd.
http://www.techno-press.org/?journal=scs&subpage=6 ISSN: 1229-9367 (Print), 1598-6233 (Online)

development of both the relevant theoretical methodologies and numerical modeling of FGM structures has thus attracted considerable attention. The literature survey in this work will focus on papers that have carried out the structural analyses of single-layered and sandwiched FGM circular plates under axisymmetric loads.

Reddy *et al*. (1999) examined the axisymmetric bending and stretching of single-layered, functionally graded (FG) annular and circular plates with different boundary conditions on the basis of the classical plate theory (CPT) and first-order shear deformation theory (FSDT). The plate was considered to be composed of Titanium (metal) and Zirconia (ceramic) materials according to a power-law distribution of their volume fractions varying through the thickness coordinate, and the effective material properties of the plate were estimated by using the rule of mixtures (Lei *et al*. 2013, Zhu *et al*. 2012). The FSDT was also used to examine the free vibration characteristics of moderately thick FGM annular plates integrated with surface-bonding piezoelectric layers by Ebrahimi *et al*. (2009), and the static behavior of laminated composite rectangular and annular plates was investigated by Tornabene *et al*. (2012), in which the differential quadrature (DQ) method was used to obtain the numerical solutions of field variables, and their results were in good agreement with the three-dimensional (3D) finite element method. Based on the third-order shear deformation theory (TSDT), Ma and Wang (2004) and Saidi *et al*. (2009) undertook the axisymmetric bending and buckling analyses of FGM circular plates. In Ma and Wang, the relationships between their solutions for FGM circular plates and those for isotropic ones were examined and compared with each other, while in Saidi *et al*. the shear-free conditions on the top and bottom surfaces of the plate were released, which is particularly useful for cases when the plate is subjected to contact friction. A number of other studies related to the structural analyses of FGM circular plates using the two-dimensional (2D) plate theories can also be found, such as elastostatic (Civalek and Ulker 2004), vibration and mechanical buckling (Lal and Ahlawat 2015), thermal buckling (Kiani and Eslami 2013), thermal bending (Hamzehkolaei *et al*. 2011) and nonlinear bending (Reddy and Berry 2012) analyses.

However, there are relatively few articles with regard to 3D analyses of axisymmetric bending problems of FGM circular plates in the open literature, as compared with those examined by various 2D plate theories. This is mainly due to the fact that the mathematical derivation of 3D approaches is considerably more complicated and difficult to apply in engineering applications, even though the results of such methods can be useful in realizing the true structural characteristics of plates. Within the framework of 3D elasticity theory, Li *et al*. (2008) presented the analytical solutions of transversely isotropic FGM circular plates subjected to an axisymmetric transverse load, in which the material properties are considered to obey an exponent-law exponentially varying through the thickness coordinate. The above-mentioned problem was also analyzed by Wang *et al*. (2010a) using the direct displacement method and by Lu *et al*. (2016) using Plevako's approach (Plevako 1971).

As mentioned above, the 3D approaches involve complicated mathematical derivations, while the 2D ones might not accurately capture the true structural characteristics. A compromise between these two approaches, the so-called semi-analytical numerical method, has thus been developed for the structural analysis of single- and multi-layered FGM plates and shells. A comprehensive literature survey with regard to the 3D semi-analytical numerical methods for the analysis of FGM plates and shells was carried out by Wu and Liu (2016), in which assorted combinations of analytical methods, such as the state space (SS) (Chen *et al*. 2001, Chen and Wang 2002, Pan 2003, Pan and Heyliger 2003, Wu and Liu 2007) and perturbation (Wu and Jiang 2015a, b) methods, and numerical methods, such as the finite element (Wu and Chang 2012, Wu and Li 2010, 2013a, b), meshless (Wang *et al*. 2010a, Chen *et al*. 2011) and differential quadrature (DQ) (Liang *et al*. 2014, 2015, Nie and Zhong 2007, 2010) methods, were introduced. Among these semi-analytical numerical methods, the SS meshless method using the differential reproducing kernel (DRK) seems to function well for the FGM sandwich circular hollow cylinders (Wu and Jiang 2012, 2014), and it is thus adopted in this work.

In the formulation of this work, the Euler-Lagrange equations, related to the 3D axisymmetric bending problems of FGM circular plates, and their associated possible boundary conditions, are derived using Reissner's mixed variational theorem (RMVT) (Reissner 1984, 1986). The DRK interpolation functions (Wang *et al*. 2010a) are used to interpolate the primary field variables in the axial coordinate, and two different edge conditions, simply-supported and clamped ones, are considered. By substituting these DRK interpolants into the strong formulation of this problem, we thus obtain the system SS equations of the plates with simply-supported and clamped edges. Finally, the through-thickness distributions of these field variables can be determined using a transfer matrix method (Wu and Li 2016, Wu and Tsai 2012), in which the general solutions of the system equations can be calculated layer-by-layer, which is significantly less time-consuming than the usual approach. Moreover, a parametric study with regard to the influence of the boundary conditions, thickness-to-radius ratio, and material-property gradient index on the assorted field variables induced in the FGM sandwich circulate plates is undertaken. Some physical observations for the plates with regard to the reduction of transverse stress at the face sheet-core interfaces and smooth distributions of the interlaminar stresses across these interfaces are also reported.

2. RMVT-based state space equations

2.1 Reissner's energy functional

We consider a multilayered FGM axisymmetric circular plate with simply-supported and clamped edges, and subjected to a uniformly distributed load on the top surface, as shown in Fig. 1. A global polar coordinate system (r, θ and ζ coordinates) is adopted and located at the center of the plate. A set of local thickness coordinates, z_m (m = 1, 2, ..., N_l), is located at the middle surface of each individual layer, respectively, where N_l denotes the total number of layers constituting the plate. The radius of the plate is defined as a. The thicknesses of each individual layer and the plate are h_m (m = 1, 2, ..., N_l) and h, respectively, while $h = \sum_{m=1}^{N_l} h_m$. The relationship between the global and local thickness coordinates in the mth-layer is $\zeta = \bar{\zeta}_m + z_m$, in which $\bar{\zeta}_m = (\zeta_m + \zeta_{m-1})/2$, and ζ_m and ζ_{m-1} are the global thickness coordinates measured from the middle surface of the plate to the top and bottom surfaces of the mth-layer, respectively.

For an axisymmetric circular plate, the field variables must be independent of the circumferential coordinate (θ), such that their derivatives with respect to this are zeroes, and the displacement component in the θ direction (u_θ) remains zero when the plate is subjected to an axisymmetric load. In addition, the strain components $\gamma_{r\theta}$ and $\gamma_{\zeta\theta}$ are zeroes, and the stress components $\tau_{r\theta}$ and $\tau_{\zeta\theta}$ are thus zeroes for an orthotropic material plate.

The linear constitutive equations valid for the nature of the symmetry class of elastic materials are given by (Reddy *et al*. 1999, Li *et al*. 2008).

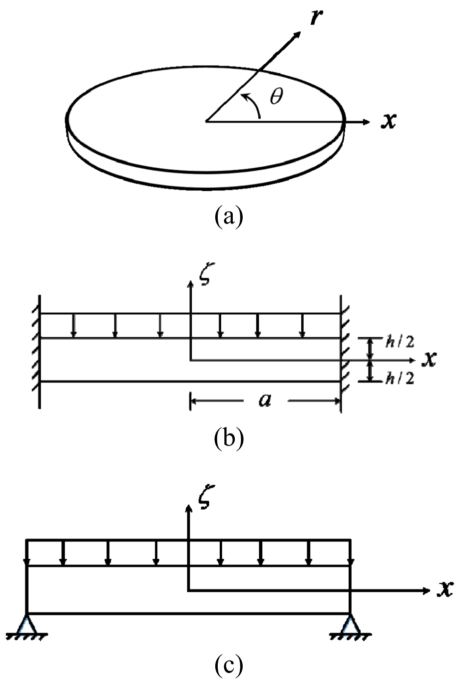

Fig. 1 An FGM circular plate with simply-supported and clamped edges and under uniform loads. (a) The configuration and polar coordinate system; (b) A simply-supported circular plate; (c) A clamped circular plate

$$\begin{Bmatrix} \sigma_r^{(m)} \\ \sigma_\theta^{(m)} \\ \sigma_\zeta^{(m)} \\ \tau_{r\zeta}^{(m)} \end{Bmatrix} = \begin{bmatrix} c_{11}^{(m)} & c_{12}^{(m)} & c_{13}^{(m)} & 0 \\ c_{12}^{(m)} & c_{22}^{(m)} & c_{23}^{(m)} & 0 \\ c_{13}^{(m)} & c_{23}^{(m)} & c_{33}^{(m)} & 0 \\ 0 & 0 & 0 & c_{44}^{(m)} \end{bmatrix} \begin{Bmatrix} \varepsilon_r^{(m)} \\ \varepsilon_\theta^{(m)} \\ \varepsilon_\zeta^{(m)} \\ \gamma_{r\zeta}^{(m)} \end{Bmatrix}, \tag{1}$$

where ($\sigma_r^{(m)}$, $\sigma_\theta^{(m)}$, $\sigma_\zeta^{(m)}$, $\tau_{r\zeta}^{(m)}$) and ($\varepsilon_r^{(m)}$, $\varepsilon_\theta^{(m)}$, $\varepsilon_\zeta^{(m)}$, $\gamma_{r\zeta}^{(m)}$) are the nonzero stress and strain components of a certain material point in the *m*th-layer, respectively. $c_{ij}^{(m)}$ (i, j = 1 – 4) are the elastic coefficients which are constants through the thickness coordinate in the homogeneous elastic layers, and are variable through the thickness coordinate in the FGM layers (i.e., $c_{ij}^{(m)}(\zeta)$ or $c_{ij}^{(m)}(z_m)$). For the isotropic material, the coefficients c_{ij} will be expressed as $c_{11} = c_{22} = c_{33} = [(1-\upsilon)E/(1+\upsilon)(1-2\upsilon)]$, $c_{12} = c_{13} = c_{23} = [\upsilon E/(1+\upsilon)(1-2\upsilon)]$ and $c_{44} = [E/2(1+\upsilon)]$, in which E and υ are Young's modulus and Poisson's ratio, respectively.

The strain-displacement relations are

$$\begin{Bmatrix} \varepsilon_r^{(m)} \\ \varepsilon_\theta^{(m)} \\ \varepsilon_\zeta^{(m)} \\ \gamma_{r\zeta}^{(m)} \end{Bmatrix} = \begin{bmatrix} \partial_r & 0 \\ (1/r) & 0 \\ 0 & \partial_\zeta \\ \partial_\zeta & \partial_r \end{bmatrix} \begin{Bmatrix} u_r^{(m)} \\ u_\zeta^{(m)} \end{Bmatrix}, \tag{2}$$

where $u_r^{(m)}$ and $u_\zeta^{(m)}$ denote the elastic displacement components in the radial (r) and thickness (ζ) directions, respectively, and $\partial_k = \partial / \partial k$ ($k = r$ and ζ).

The Reissner energy functional related to this 3D analysis of multilayered FGM axisymmetric circular plates is written in the form of (Reissner 1984, 1986)

$$\begin{aligned}\Pi_R &= 2\pi \sum_{m=1}^{N_l} \int_{-h_m/2}^{h_m/2} \int_0^a \left[\sigma_r^{(m)}\, \varepsilon_r^{(m)} + \sigma_\theta^{(m)}\, \varepsilon_\theta^{(m)} + \sigma_\zeta^{(m)}\, \varepsilon_\zeta^{(m)} + \tau_{r\zeta}^{(m)}\, \gamma_{r\zeta}^{(m)} - B(\sigma_{ij}^{(m)})\right] r\, dr\; dz_m \\ &\quad - 2\pi \int_0^a \bar{q}_\zeta^{\pm}\, u_\zeta^{\pm}\, r\, dr - 2\pi a \sum_{m=1}^{N_l} \int_{-h_m/2}^{h_m/2} \bar{T}_i^{(m)}\, u_i^{(m)}\, dz_m \\ &\quad - 2\pi a \sum_{m=1}^{N_l} \int_{-h_m/2}^{h_m/2} T_i^{(m)}\, (u_i^{(m)} - \bar{u}_i^{(m)})\, dz_m,\end{aligned} \tag{3}$$

where $u_\zeta^{\pm}$ denotes the displacement components at the top and bottom surfaces of the plate, in which the transverse loads $\bar{q}_\zeta^{\pm}$ are applied, the positive directions of which are defined to be upward. Either the surface tractions $\bar{T}_i^{(m)}$ ($i = r$ and ζ) or surface displacements $\bar{u}_i^{(m)}$ ($i = r$ and ζ) are prescribed along the edge boundary, respectively. $B(\sigma_{ij}^{(m)})$ is the complementary energy density function.

In the present formulation, we take the elastic displacement ($u_r^{(m)}$ and $u_\zeta^{(m)}$) and transverse stress ($\tau_{r\zeta}^{(m)}$ and $\sigma_\zeta^{(m)}$) components as the primary variables subject to variation, and the in- and out-of-plane strain and the in-plane stress components are the dependent variables, which can be expressed in terms of the primary variables using Eqs. (1)-(2) as follows

$$\varepsilon_r^{(m)} = \partial B / \partial \sigma_r^{(m)} = u_r^{(m)},_r, \tag{4}$$

$$\varepsilon_\theta^{(m)} = \partial B / \partial \sigma_\theta^{(m)} = (1/r) u_r^{(m)}, \tag{5}$$

$$\varepsilon_\zeta^{(m)} = \partial B / \partial \sigma_\zeta^{(m)} = -\tilde{c}_{13}^{(m)}\, u_r^{(m)},_r - \left(\tilde{c}_{23}^{(m)} / r\right) u_r^{(m)} + \left(1 / c_{33}^{(m)}\right) \sigma_\zeta^{(m)}, \tag{6}$$

$$\gamma_{r\zeta}^{(m)} = \partial B / \partial \tau_{r\zeta}^{(m)} = \left(1 / c_{44}^{(m)}\right) \tau_{r\zeta}^{(m)}, \tag{7}$$

$$\boldsymbol{\sigma}_p^{(m)} = \mathbf{Q}_p^{(m)}\, \mathbf{B}_1\, u_r^{(m)} + \mathbf{Q}_\zeta^{(m)}\, \sigma_\zeta^{(m)}, \tag{8}$$

where $\boldsymbol{\sigma}_p^{(m)} = \left\{\sigma_r^{(m)} \ \ \sigma_\theta^{(m)}\right\}^T$, $\mathbf{u}^{(m)} = \left\{u_r^{(m)} \ \ u_\theta^{(m)}\right\}^T$, $\mathbf{Q}_p^{(m)} = \begin{bmatrix} Q_{11}^{(m)} & Q_{12}^{(m)} \\ Q_{12}^{(m)} & Q_{22}^{(m)} \end{bmatrix}$, $\mathbf{B}_1 = \begin{bmatrix} \partial_r \\ (1/r) \end{bmatrix}$, $\mathbf{Q}_\zeta^{(m)} = \begin{bmatrix} \tilde{c}_{13}^{(m)} \\ \tilde{c}_{23}^{(m)} \end{bmatrix}$, $Q_{ij}^{(m)} = c_{ij}^{(m)} - \left(c_{i3}^{(m)} c_{j3}^{(m)} / c_{33}^{(m)}\right)$ ($i, j = 1$ and 2), $\tilde{c}_{i3}^{(m)} = c_{i3}^{(m)} / c_{33}^{(m)}$ ($i = 1$ and 2).

2.2 Euler-Lagrange equations

Substituting Eqs. (4)-(8) into Eq. (3), then imposing the stationary principle of the Reissner energy functional (i.e., $\delta\Pi_R = 0$) and performing the Green theorem, we finally obtain

$$
\begin{aligned}
\delta\Pi_R &= (2\pi)\sum_{m=1}^{N_l} \int_{-h_m/2}^{h_m/2} \int_0^a \Big\{ [-(r\,\sigma_r^{(m)}),_r - r\,\tau_{r\zeta}^{(m)},_\zeta + \sigma_\theta^{(m)}]\,\delta u_r^{(m)} + \left[-\left(r\,\tau_{r\zeta}^{(m)}\right),_r - r\,\sigma_\zeta^{(m)},_\zeta\right]\delta u_\zeta^{(m)} \\
&\quad + r\left[u_r^{(m)},_\zeta + u_\zeta^{(m)},_r - \left(1/c_{55}^{(m)}\right)\tau_{r\zeta}^{(m)}\right]\delta\tau_{r\zeta}^{(m)} + r\left[u_\zeta^{(m)},_\zeta + \tilde{c}_{13}\,u_r^{(m)},_r + (\tilde{c}_{23}/r)\,u_r^{(m)}\right. \\
&\quad \left. - \left(1/\tilde{c}_{33}^{(m)}\right)\sigma_\zeta^{(m)}\right]\delta\sigma_\zeta^{(m)} \Big\}\,dr\,dz_m + (2\pi)\int_0^a \left\{ \begin{array}{l} r\left[\sigma_\zeta^{+} - \bar{q}_\zeta^{+}\right]\delta u_\zeta^{+} \\ + r\left[\sigma_\zeta^{-} + \bar{q}_\zeta^{-}\right]\delta u_\zeta^{-} + r\left[\tau_{r\zeta}^{\pm}\right]\delta u_r^{\pm} \end{array} \right\} dr \\
&\quad + (2\pi a)\sum_{m=1}^{N_l} \int_{-h_m/2}^{h_m/2} \left\{ \left[\sigma_r^{(m)} - \bar{T}_r^{(m)}\right]_{r=a} \delta u_r^{(m)} + \left[\tau_{r\zeta}^{(m)} - \bar{T}_\zeta^{(m)}\right]_{r=a} \delta u_\zeta^{(m)} \right\} dz_m \\
&= 0,
\end{aligned}
\tag{9}
$$

where commas denote the derivatives of the suffix variables.

Because variations of primary variables are arbitrary, their coefficients in Eq. (9) must vanish identically over the plate domain and along its boundary surfaces. We thus obtain the Euler-Lagrange equations of FGM axisymmetric circular plates from the domain integral terms and the admissible boundary conditions from the boundary integral terms, which are written as follows:

The Euler-Lagrange equations are

$$\delta u_r^{(m)}: \qquad \tau_{r\zeta}^{(m)},_{z_m} = -\sigma_r^{(m)},_r - \left(\sigma_r^{(m)}/r\right) + \left(\sigma_\theta^{(m)}/r\right), \tag{10}$$

$$\delta u_\zeta^{(m)}: \qquad \sigma_\zeta^{(m)},_{z_m} = -\tau_{r\zeta}^{(m)},_r - \left(\tau_{r\zeta}^{(m)}/r\right), \tag{11}$$

$$\delta\tau_{r\zeta}^{(m)}: \qquad u_r^{(m)},_{z_m} = -u_\zeta^{(m)},_r + \left(\tau_{r\zeta}^{(m)}/c_{44}^{(m)}\right), \tag{12}$$

$$\delta\sigma_\zeta^{(m)}: \qquad u_\zeta^{(m)},_{z_m} = -\tilde{c}_{13}^{(m)}\,u_r^{(m)},_r - \left(\tilde{c}_{23}^{(m)}/r\right)u_r^{(m)} + \left(1/c_{33}^{(m)}\right)\sigma_\zeta^{(m)}, \tag{13}$$

where $m = 1, 2, ..., N_l$.

The top and bottom boundary conditions are

$$\left[\tau_{r\zeta}^{(N_l)} \ \ \sigma_\zeta^{(N_l)}\right] = \left[0 \quad \bar{q}_\zeta^{+}\right] \quad \text{on} \quad z_{N_l} = h_{N_l}/2 \quad (\text{or} \ \ \zeta = h/2), \tag{14a}$$

$$\left[\tau_{x\zeta}^{(1)} \ \ \sigma_\zeta^{(1)}\right] = \left[0 \quad -\bar{q}_\zeta^{-}\right] \quad \text{on} \quad z_1 = -h_1/2 \quad (\text{or} \ \ \zeta = -h/2); \tag{14b}$$

And the edge boundary conditions are

$$\tau_{r\zeta}^{(m)} = \bar{T}_\zeta^{(m)} \qquad \text{or} \qquad u_\zeta^{(m)} = \bar{u}_\zeta^{(m)}, \tag{15a}$$

$$\sigma_r^{(m)} = \bar{T}_r^{(m)} \qquad \text{or} \qquad u_r^{(m)} = \bar{u}_r^{(m)}, \tag{15b}$$

where $m = 1, 2, ..., N_l$.

The set of Euler-Lagrange Equations (Eqs. (10)-(13)) associated with a set of appropriate boundary conditions (Eqs. (15a) and (15b)) is composed of a well-posed boundary value problem, which is the so-called strong formulation of this axisymmetric problem.

3. The DRK interpolation

In this article, an SS DRK method will be developed on the basis of the above-mentioned strong formulation in combination with the DRK interpolation (Wang *et al*. 2010a) for the analysis of multilayered FGM axisymmetric circular plates with simply-supported and clamped edges and under axisymmetric mechanical loads.

The DRK interpolation functions and their relevant derivatives are briefly described, as follows.

3.1 DRK interpolation functions

It is assumed that there are n_p discrete nodes randomly selected and located at $r = r_1, r_2, ..., r_{n_p}$, respectively, in the r direction of the mth-layer, in which a function $F\,(r, z_m)$ is interpolated as $F^a\,(r, z_m)$ and defined as

$$\begin{aligned} F^a(r,\ z_m) &= \sum_{l=1}^{n_p} \psi_l(r)\ F_l(z_m) \\ &= \sum_{l=1}^{n_p} \left[\bar{\phi}_l(r)+\hat{\phi}_l(r)\right] F_l(z_m), \end{aligned} \tag{16}$$

where $\bar{\phi}_l(r)$ ($l = 1, 2,\ldots, n_p$) denote the enrichment functions, which are determined by imposing the nth-order reproducing conditions and are given by $\bar{\phi}_l(r) = w_a(r-r_l)\,\mathbf{P}^T(r-r_l)\,\bar{\mathbf{b}}(r)$, in which $\mathbf{P}^T(r-r_l) = \left[1\ (r-r_l)\ (r-r_l)^2\ \cdots\ (r-r_l)^n\right]$, n is the highest order of the base functions, $\bar{\mathbf{b}}(r)$ is the undetermined function vector, and $w_a\,(r - r_l)$ is the weight function centered at the node, $r = r_l$, with a support size a_r; $\hat{\phi}_l(r)$ ($l = 1, 2, \ldots, n_p$) denote the primitive functions, which are used to introduce the Kronecker delta properties; $\psi_l\,(r)$ is the shape function of $F^a\,(r, z_m)$ at the sampling node, $r = r_l$; and $F_l\,(z_m)$ is the nodal function of $F^a\,(r, z_m)$ at $r = r_l$.

By selecting the complete n^{th}-order polynomials as the base functions to be reproduced, we obtain a set of reproducing conditions to determine the undetermined functions of $\bar{b}_i(r)$ ($i = 1, 2, \cdots, n+1$) in Eq. (16). These conditions are given as

$$\sum_{l=1}^{n_p} \left[\, \bar{\phi}_l(r)+\hat{\phi}_l(r)\,\right]\, x_l^i = x^i \qquad i \le n\,. \tag{17}$$

Eq. (17) represents $(n + 1)$ reproducing conditions, and the matrix form of these is given as

$$\begin{aligned} \sum_{l=1}^{n_p} \mathbf{P}(r-r_l)\,\bar{\phi}_l(r) &= \sum_{l=1}^{n_p} \mathbf{P}(r-r_l)\, w_a(r-r_l)\,\mathbf{P}^T(r-r_l)\,\bar{\mathbf{b}}(r) \\ &= \mathbf{P}(\mathbf{0}) - \sum_{l=1}^{n_p} \mathbf{P}(r-r_l)\,\hat{\phi}_l(r), \end{aligned} \tag{18}$$

where $\mathbf{P}(\mathbf{0}) = [1\ 0\ 0\ \cdots\ 0]^T$.

According to these conditions, we may obtain the undetermined function vector $\overline{\mathbf{b}}(r)$ in the following form

$$\overline{\mathbf{b}}(r) = \mathbf{A}^{-1}(r)\left[\mathbf{P}(\mathbf{0}) - \sum_{l=1}^{n_p} \mathbf{P}(r - r_l)\,\hat{\phi}_l(r)\right], \tag{19}$$

where $\mathbf{A}(r) = \sum_{l=1}^{n_p} \mathbf{P}(r - r_l)\, w_a(r - r_l)\, \mathbf{P}^T(r - r_l)$.

Substituting Eq. (19) into Eq. (16) yields the shape functions of F^a (r, z_m) in the form of

$$\psi_l(r) = \overline{\phi}_l(r) + \hat{\phi}_l(r) \qquad (i = 1, 2, \cdots, n_p), \tag{20}$$

where $\overline{\phi}_l(r) = w_a(r - r_l)\mathbf{P}^T(r - r_l)\mathbf{A}^{-1}(r)\left[\mathbf{P}(\mathbf{0}) - \sum_{l=1}^{n_p} \mathbf{P}(r - r_l)\hat{\phi}(r)\right]$.

It is noted that if we select a set of primitive functions satisfying the Kronecker delta properties (i.e., $\hat{\phi}_l(r_k) = \delta_{lk}$), *a priori*, then a set of the shape functions with these properties will be obtained (i.e., $\psi_l(r_k) = \delta_{lk}$) due to the fact that the enrichment functions vanish at all the nodes (i.e., $\overline{\phi}_l(r_k) = 0$). In this article, a quartic spline function with its support size not covering any neighboring nodes, as suggested by Wang *et al.* (2010a), is assigned to be the primitive function for each sampling node.

It is realized from Eq. (20) that ψ_l (r) vanishes when r is not in the support of the node at $r = r_l$. The influence of the shape functions in the support of the referred node monotonically decreases when the relative distance to the node increases, and this preserves the local character of the present scheme. The derivatives of these DRK interpolation functions may be found in Wang *et al.* (2010a), and thus are not repeated here.

3.2 Weight functions

In implementing the present scheme, the weight and primitive functions (i.e., $w(s)$ and $\hat{\phi}(s)$) must be selected in advance. According to Wang *et al.* (2010a), the normalized Gaussian function is selected as the weight function at each sampling node, and this is given as

$$w(s) = \begin{cases} \dfrac{e^{-(s/\alpha)^2} - e^{-(1/\alpha)^2}}{1 - e^{-(1/\alpha)^2}} & \text{for} \quad s \le 1 \\ 0 & \text{for} \quad s > 1 \end{cases}, \tag{21}$$

where w_a $(r - r_l) = w(s)$ and $s = |r - r_l| / a_r$, in which a_r is the radius of the influence zone (or the support size), and α is set as 0.3.

The quartic spline function is selected as the primitive function at each sampling node and given as

$$\hat{\varphi}(s) = \begin{cases} -3s^4 + 8s^3 - 6s^2 + 1 & \text{for} \quad s \le 1 \\ 0 & \text{for} \quad s > 1 \end{cases}, \tag{22}$$

4. A state space DRK method

In conjunction with the DRK interpolation and state space method, we develop a state space DRK method to study the 3D axisymmetric bending behaviors of FGM circular plates with simply-supported and clamped edges. The loading conditions on the top and bottom surfaces and edge boundary conditions of the circular plate are given as follows.

In this analysis, only the transverse normal loads applied on the top surface of the plate are considered, other tractions are free, and given by

$$\bar{q}_\zeta^+ = \bar{q}_\zeta^+(r), \tag{23a}$$

$$\text{and} \qquad \bar{q}_\zeta^- = 0. \tag{23b}$$

The symmetric conditions at $r = 0$ are given by

$$u_r^{(m)} = \tau_{r\zeta}^{(m)} = 0 \qquad (m = 1, 2, \cdots, N_l), \tag{24}$$

The edge boundary conditions of the plates are considered as simply-supported and clamped edges and are written as follows:

Case 1. Simply-supported edge

$$u_\zeta^{(m)} = \sigma_r^{(m)} = 0 \qquad \text{at} \qquad r = a\,, \tag{25}$$

Case 2. Clamped edge

$$u_\zeta^{(m)} = u_r^{(m)} = 0 \qquad \text{at} \qquad r = a\,, \tag{26}$$

where $m = 1, 2, ..., N_l$ in the above-mentioned cases.

4.1 The state space equations

Substituting the DRK formula (Eq. (16)) and those of their derivatives in the strong formulation of this axisymmetric problem, that consists of the Euler-Lagrange Equations (i.e., Eqs. (10)-(13)) associated with the symmetric conditions at $r = 0$ (i.e., Eq. (24)) and appropriate boundary conditions of Cases 1 and 2 given in Eqs. (25)-(26), we obtain the following sets of ordinary differential equations:

Case 1. Simply-supported edge

Satisfying the symmetric conditions at $r = 0$ (Eq. (24) and edge conditions at r = a (Eq. (25)) yields

$$\left(u_r^{(m)}\right)_1 = \left(\tau_{r\zeta}^{(m)}\right)_1 = 0, \tag{27a}$$

$$\left(u_\zeta^{(m)}\right)_{n_p} = 0\,, \text{ and } \left(\sigma_\zeta^{(m)}\right)_{n_p} = -\left(Q_{11}^{(m)} / \tilde{c}_{13}^{(m)}\right)\sum_{j=2}^{n_p} \psi_j^{(1)}\left(r_{n_p}\right)\left(u_r^{(m)}\right)_j - \left[Q_{12}^{(m)} / \left(\tilde{c}_{13}^{(m)} r_{n_p}\right)\right]\left(u_r^{(m)}\right)_{n_p}\,. \tag{27b}$$

Using Eqs. (27a) and (27b), we write the Euler-Lagrange equations as follows

$$\left(u_r^{(m)}\right)_{i},_{z_m} = -\sum_{j=1}^{(n_p-1)} \left[\psi_j^{(1)}(r_i)\right]\left(u_\zeta^{(m)}\right)_j + \left(1/c_{44}^{(m)}\right)\left(\tau_{r\zeta}^{(m)}\right)_i \qquad \left(i = 2, \cdots, n_p\right), \tag{28}$$

$$\left(u_\zeta^{(m)}\right)_{i},_{z_m} = -\tilde{c}_{13}^{(m)} \sum_{j=2}^{n_p} \left[\psi_j^{(1)}(r_i)\right]\left(u_r^{(m)}\right)_j - \left(1-\delta_{i1}\right)\left(\tilde{c}_{23}^{(m)}/r_i\right)\left(u_r^{(m)}\right)_i + \left(1/c_{33}^{(m)}\right)\left(\sigma_\zeta^{(m)}\right)_i \qquad \left(i = 1, 2, \cdots, \left(n_p-1\right)\right), \tag{29}$$

$$\begin{aligned}\left(\tau_{r\zeta}^{(m)}\right)_{i},_{z_m} = &-Q_{11}^{(m)} \sum_{j=2}^{n_p} \left[\psi_j^{(2)}(r_i) + \psi_j^{(1)}(r_i)/r_i\right]\left(u_r^{(m)}\right)_j + \left(Q_{22}^{(m)}/r_i^2\right)\left(u_r^{(m)}\right)_i \\ &-\tilde{c}_{13}^{(m)} \sum_{j=1}^{n_p-1} \left[\psi_j^{(1)}(r_i)\right]\left(\sigma_\zeta^{(m)}\right)_j - \left(1-\delta_{in_p}\right)\left[\left(\tilde{c}_{13}^{(m)} - \tilde{c}_{23}^{(m)}\right)/r_i\right]\left(\sigma_\zeta^{(m)}\right)_i \\ &+\tilde{c}_{13}^{(m)}\left[\psi_{n_p}^{(1)}(r_i)\right]\left[\sum_{j=2}^{n_p}\left(Q_{11}^{(m)}/\tilde{c}_{13}^{(m)}\right)\psi_j^{(1)}\left(r_{n_p}\right)\left(u_r^{(m)}\right)_j + \left(Q_{12}^{(m)}\left(u_r^{(m)}\right)_{n_p}\right)/\left(\tilde{c}_{13}^{(m)} r_{n_p}\right)\right] \\ &+\delta_{in_p}\left[\left(\tilde{c}_{13}^{(m)} - \tilde{c}_{23}^{(m)}\right)/r_i\right]\left[\sum_{j=2}^{n_p}\left(Q_{11}^{(m)}/\tilde{c}_{13}^{(m)}\right)\psi_j^{(1)}\left(r_{n_p}\right)\left(u_r^{(m)}\right)_j + \left(Q_{12}^{(m)}\left(u_r^{(m)}\right)_{n_p}\right)/\left(\tilde{c}_{13}^{(m)} r_{n_p}\right)\right] \\ &\left(i = 2, 3, \cdots, n_p\right),\end{aligned} \tag{30}$$

$$\left(\sigma_\zeta^{(m)}\right)_{i},_{z_m} = -\sum_{j=2}^{n_p} \left[\psi_j^{(1)}(r_i)\right]\left(\tau_{r\zeta}^{(m)}\right)_j - \left(1-\delta_{i1}\right)\left(1/r_i\right)\left(\tau_{r\zeta}^{(m)}\right)_i \qquad \left(i = 1, 2, \cdots, \left(n_p-1\right)\right), \tag{31}$$

where δ_{kl} is the Dirac delta function, in which $\delta_{kl} = 0$ when $k \neq l$, and $\delta_{kl} = 1$ when $k = l$.

Case 2. Clamped edge

Satisfying the symmetric conditions at $r = 0$ (Eq. (24) and edge conditions at $r = a$ (Eq. (26)) yields

$$\left(u_r^{(m)}\right)_1 = \left(\tau_{r\zeta}^{(m)}\right)_1 = 0\,, \tag{32a}$$

$$\left(u_r^{(m)}\right)_{n_p} = \left(u_\zeta^{(m)}\right)_{n_p} = 0\,, \tag{32b}$$

Using Eqs. (32a) and (32b), we write the Euler-Lagrange equations as follows

$$\left(u_r^{(m)}\right)_{i},_{z_m} = -\sum_{j=1}^{(n_p-1)} \left[\psi_j^{(1)}(r_i)\right]\left(u_\zeta^{(m)}\right)_j + \left(1/c_{44}^{(m)}\right)\left(\tau_{r\zeta}^{(m)}\right)_i \qquad \left(i = 2, 3, \cdots, n_p\right), \tag{33}$$

$$\left(u_\zeta^{(m)}\right)_{i},_{z_m} = -\tilde{c}_{13}^{(m)} \sum_{j=2}^{(n_p-1)} \left[\psi_j^{(1)}(r_i)\right]\left(u_r^{(m)}\right)_j - (1-\delta_{i1})\left(1-\delta_{in_p}\right)\left(\tilde{c}_{23}^{(m)}/r_i\right)\left(u_r^{(m)}\right)_i + \left(1/c_{33}^{(m)}\right)\left(\sigma_\zeta^{(m)}\right)_i \quad \left(i = 1, 2, \cdots, n_p\right), \tag{34}$$

$$\begin{aligned}\left(\tau_{r\zeta}^{(m)}\right)_{i},_{z_m} = &-Q_{11}^{(m)} \sum_{j=2}^{(n_p-1)} \left[\psi_j^{(2)}(r_i) + \psi_j^{(1)}(r_i)/r_i\right]\left(u_r^{(m)}\right)_j + \left(Q_{22}^{(m)}/r_i^2\right)\left(u_r^{(m)}\right)_i \\ &- \tilde{c}_{13}^{(m)} \sum_{j=1}^{n_p} \left[\psi_j^{(1)}(r_i)\right]\left(\sigma_\zeta^{(m)}\right)_j - \left[\left(\tilde{c}_{13}^{(m)} - \tilde{c}_{23}^{(m)}\right)/r_i\right]\left(\sigma_\zeta^{(m)}\right)_i\end{aligned} \quad \left(i = 2, 3, \cdots, \left(n_p - 1\right)\right), \tag{35}$$

$$\left(\sigma_\zeta^{(m)}\right)_{i},_{z_m} = -\sum_{j=2}^{n_p} \left[\psi_j^{(1)}(r_i)\right]\left(\tau_{r\zeta}^{(m)}\right)_j - (1-\delta_{i1})(1/r_i)\left(\tau_{r\zeta}^{(m)}\right)_i \qquad \left(i = 1, 2, \cdots, \left(n_p - 1\right)\right), \tag{36}$$

Eqs. (28)-(31) and (33)-(36) represent the systems of SS equations for the m^{th}-layer of the FGM axisymmetric circular plates with edge conditions of Cases 1 and 2, respectively, in which each system consists of $(4n_p - 4)$ simultaneously linear ordinary differential equations (ODEs) in terms of $(4n_p - 4)$ primary variables. These SS equations for Cases 1 and 2 are rewritten in the matrix form as follows

$$\frac{d\,\mathbf{F}^{(m)}}{d\,z_m} = \mathbf{K}^{(m)}\,\mathbf{F}^{(m)} \qquad m = 1, 2, \cdots, N_l\,, \tag{37}$$

in which $\mathbf{F}^{(m)}$ and $\mathbf{K}^{(m)}$ denote the state space variables and the corresponding coefficient matrix of the mth-layer of the circular plate, respectively. For Case 1

$$\mathbf{F}^{(m)} = \left\{\left(u_r^{(m)}\right)_2 \cdots \left(u_r^{(m)}\right)_{n_p} \left(u_\zeta^{(m)}\right)_1 \cdots \left(u_\zeta^{(m)}\right)_{n_p-1} \left(\tau_{r\zeta}^{(m)}\right)_2 \cdots \left(\tau_{r\zeta}^{(m)}\right)_{n_p} \left(\sigma_\zeta^{(m)}\right)_1 \cdots \left(\sigma_\zeta^{(m)}\right)_{n_p-1}\right\}^T,$$

and for Case 2 $\mathbf{F}^{(m)} = \{(u_r^{(m)})_2 \cdots (u_r^{(m)})_{n_p-1} (u_\zeta^{(m)})_1 \cdots (u_\zeta^{(m)})_{n_p-1} (\tau_{r\zeta}^{(m)})_2 \cdots (\tau_{r\zeta}^{(m)})_{n_p} (\sigma_\zeta^{(m)})_1 \cdots \left(\sigma_\zeta^{(m)}\right)_{n_p}\}^T$.

4.2 Theories of the homogeneous linear systems

The general solution of Eq. (37) is

$$\mathbf{F}^{(m)}(z_m) = \mathbf{\Omega}^{(m)}(z_m)\,\mathbf{L}^{(m)}, \tag{38}$$

where $\mathbf{L}^{(m)}$ is a $(4n_p - 4) \times 1$ matrix of arbitrary constants; $\mathbf{\Omega}^{(m)}$ is a fundamental matrix of Eq. (37), and is formed by $(4n_p - 4)$ linearly independent solutions in the form of $\mathbf{\Omega}^{(m)} = [\mathbf{\Omega}_1^{(m)},\ \mathbf{\Omega}_2^{(m)}, \cdots,\ \mathbf{\Omega}_{(4n_p-4)}^{(m)}]$, $\mathbf{\Omega}_i^{(m)} = \mathbf{\Lambda}_i\, e^{\lambda_i z_m}$ $(i = 1, 2, \cdots, (4n_p - 4))$; λ_i and $\mathbf{\Lambda}_i$ are the eigenvalues and their corresponding eigenvectors of the coefficient matrix $\mathbf{K}^{(m)}$ in Eq. (37), respectively.

On the basis of the previous set of linearly independent real-valued solutions, a transfer matrix method can be developed for the analysis of FGM axisymmetric circular plates using the successive integration method (Soldatos and Hadjigeorgiou 1990), where each FGM layer of the circular plate is artificially divided into a finite number of individual layers with an equal and small thickness for each layer, compared with the radius (a), as well as with constant material properties, determined in an average thickness sense. The exact solutions of the assorted field variables induced in the FGM axisymmetric circular plate with simply-supported and clamped edge conditions can thus be gradually approached by increasing the number of individual layers. It is noted that this solution process can be performed layer-by-layer, and the computational performance is independent of the total number of individual layers. Consequently, the implementation of the present approach is much less time-consuming than usual.

4.3 The transfer matrix method

A transfer matrix method for the 3D analysis of FGM axisymmetric circular plates with simply-supported and clamped edges is then developed as follows, in which the FGM cylinder is artificially divided into an N_l-layered ccircular plate with an equal and small thickness compared with its radius. According to Eq. (38), we may obtain the general solution for the state space equations of the mth-layer (m = 1, 2, ..., N_l).

When $z_m = -h_m / 2$, we thus obtain

$$\mathbf{L}^{(m)} = \left[\mathbf{\Omega}^{(m)}\left(-h_m/2\right)\right]^{-1}\mathbf{F}_{(m-1)}, \tag{39}$$

where $\mathbf{F}_{(m-1)}$ denotes the vector of state space variables at the interface between the $(m\text{-}1)^{\text{th}}$- and m^{th}-layers, and $\mathbf{F}_{(m-1)} = \mathbf{F}^{(m)}\left(z_m = -h_m/2\right)$.

Using Eqs. (38) and (39), we obtain

$$\mathbf{F}_{(m)} = \mathbf{R}_{(m)}\,\mathbf{F}_{(m-1)}, \tag{40}$$

where $\mathbf{R}_{(m)} = \mathbf{\Omega}^{(m)}\left(z_m\right)\left[\mathbf{\Omega}^{(m)}\left(-h_m/2\right)\right]^{-1}$.

By analogy, the vectors of state space variables between the top and bottom surfaces of the cylinder (i.e., $\mathbf{F}_{(N_l)}$ and $\mathbf{F}_{(0)}$) are linked by

$$\begin{aligned}\mathbf{F}_{(N_l)} &= \mathbf{R}_{(N_l)}\,\mathbf{F}_{(N_l-1)}\\ &= \left(\prod_{m=1}^{N_l}\mathbf{R}_{(m)}\right)\mathbf{F}_{(0)}.\end{aligned} \tag{41}$$

where $\prod_{m=1}^{N_l}\mathbf{R}_{(m)} = \mathbf{R}_{(N_l)}\,\mathbf{R}_{(N_l-1)}\cdots\mathbf{R}_{(2)}\,\mathbf{R}_{(1)}$.

Eq. (41) represents a set of $(4n_p - 4)$ simultaneous algebraic equations. Imposing the prescribed loading conditions on the top and buttom surfaces, we may determine the other unknown state space variables on these surfaces. The values of these primary variables through the thickness coordinate of the circular plate can then be obtained by

$$\mathbf{F}^{(1)}(z_m) = \mathbf{\Omega}^{(1)}\left(z_m\right)\left[\mathbf{\Omega}^{(1)}\left(-h_1/2\right)\right]^{-1}\mathbf{F}_{(0)}, \tag{42}$$

and $$\mathbf{F}^{(m)}(z_m) = \mathbf{\Omega}^{(m)}\left(z_m\right)\left[\mathbf{\Omega}^{(m)}\left(-h_m/2\right)\right]^{-1}\mathbf{F}_{(m-1)}, \tag{43}$$

where $\mathbf{F}_{(m-1)} = \mathbf{R}_{(m-1)}\mathbf{F}_{(m-2)}$ and m = 2, 3, ..., N_l.

Once the state space variables varying through the thickness of the circular plate are determined, the corresponding set of through-thickness distributions of dependent variables can then be obtained using Eqs. (42)-(43).

5. Illustrative examples

5.1 Single-layered FGM circular plates

Reddy *et al*. (1999) presented the accurate solutions for single-layered, isotropic FGM circular plates with simply-supported and clamped edges, and subjected to the uniformly distributed load ($\bar{q}_\zeta^+ = q_0$ and $\bar{q}_\zeta^- = 0$) by using the CPT and FSDT, in which the shear correction factor was taken to be 5/6. These accurate 2D solutions are used to validate the accuracy and convergence of this SS DRK method. The circular plates are composed of ceramic and metal materials according to a power-law distribution of volume fractions of constituents through the thickness coordinate. The effective material properties are estimated by using the rule of mixtures, in which the Poisson's ratio υ remains a constant (i.e., $\upsilon = 0.288$), while Young's modulus is in the form of

$$E(\zeta) = E_c + (E_m - E_c)\,\Gamma_m(\zeta), \tag{44}$$

where $\Gamma_m(\zeta)$ denotes the volume fraction of the metal material, and $\Gamma_m(\zeta) = [(1/2) - (\zeta/h)]^{\hat{\kappa}_p}$. E_m and E_c stand for Young's moduli of the metal and ceramic materials, respectively, and the ratio of E_m / E_c is taken to be 0.396 in the following examples. The superscript, $\hat{\kappa}_p$, denotes the material-property gradient index. When $\hat{\kappa}_p = 0$ and $\hat{\kappa}_p = \infty$, the FGM plate will reduce to the homogeneous metal and ceramic plates, respectively, while in the cases of other values of $\hat{\kappa}_p$, the top and bottom surfaces of the FGM plate are ceramic- and metal-rich, respectively, and its Young's modulus is dependent upon the thickness coordinate of the plate, as shown in Fig. 2.

Table 1 shows the convergence studies for the SS DRK solutions of the displacement components at the center of single-layered homogeneous ceramic circular plates (i.e., $\hat{\kappa}_p = 0$) with clamped boundary conditions and under a uniform load, and this problem was also examined by Sahraee and Saidi (2009) using the fourth-order shear deformation theory (FOSDT) and Reddy's third-order shear deformation theory (TSDT) (Reddy 1984a, b). The dimensionless displacement is defined as $\bar{u}_\zeta = (64 D_c / q_0 a^4) u_\zeta$, in which $D_c = (E_c h^3)/[12(1-\upsilon^2)]$. hen using the SS DRK method, the total number of artificial layers (N_l) is taken to be N_l = 2 and 10, the uniform distribution of nodes (n_p) along the radial direction of the plate is n_p = 9, 13, 17, 19 and 21, and the highest order of the base functions (n) and radius of the influence zone for each sampling node (a_r) are (n, a_r) = (3, 3.1 Δr), (3, 3.6 Δr), (4, 4.1 Δr) and (4, 4.6 Δr), in which $\Delta r = a / (n_p - 1)$. It can be seen in Table 1 that the SS DRK solutions are accurate and converge rapidly, and the solutions obtained using (n, a_r) = (3, 3.1 Δr) and (4, 4.1 Δr) are slightly more accurate than those obtained using (n, a_r) = (3, 3.6 Δr) and (4, 4.6 Δr), when we compare these SS DRK solutions with those obtained using the TSDT and FOSDT. (n, a_r) = (3, 3.1 Δr) is thus used in the following examples. In addition, because the circular plate is a homogeneous one in Table 1, the SS DRK solutions obtained using different values of N_l should remain the same as each other, and this is found in our results.

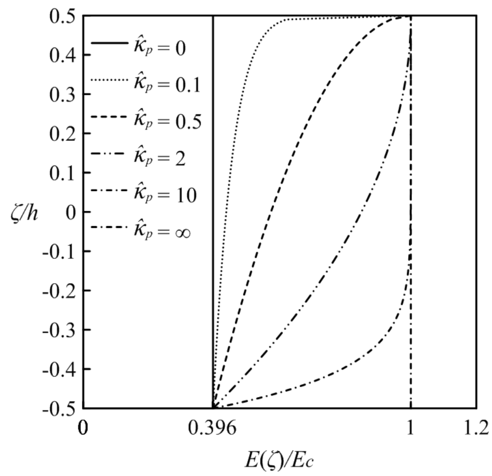

Fig. 2 The through-thickness distributions of material properties for a single-layered FGM circular plate with different values of the material-property gradient index

Table 1 Convergence studies for state space DRK solutions of the displacement components at the center of single-layered homogeneous circular plates with clamped boundary conditions and under a uniformly distributed load, in which $\hat{\kappa}_p = 0$

(n, a_r)	Theories	N_1	n_p	$h/a = 0.05$	$h/a = 0.1$	$h/a = 0.15$	$h/a = 0.2$	$h/a = 0.3$
			9	2.590	2.681	2.831	3.038	3.618
			13	2.571	2.659	2.805	3.006	3.574
		2	17	2.564	6.651	2.794	2.991	3.545
			19	2.562	2.648	2.790	2.985	3.529
			21	2.560	2.646	2.786	2.979	3.510
$(3, 3.1\Delta r)$	Present		9	2.590	2.681	2.831	3.038	3.618
			13	2.571	2.659	2.805	3.006	3.574
		10	17	2.564	6.651	2.794	2.991	3.545
			19	2.562	2.648	2.790	2.985	3.529
			21	2.560	2.646	2.786	2.979	3.510
			9	2.590	2.680	2.830	3.040	3.627
			13	2.571	2.660	2.807	3.010	3.577
		2	17	2.564	2.652	2.795	2.993	3.551
			19	2.562	2.649	2.791	2.987	3.539
			21	2.560	2.647	2.787	2.982	3.525
$(3, 3.6\Delta r)$	Present		9	2.590	2.680	2.830	3.040	3.627
			13	2.571	2.660	2.807	3.010	3.577
		10	17	2.564	2.652	2.795	2.993	3.551
			19	2.562	2.649	2.791	2.987	3.539
			21	2.560	2.647	2.787	2.982	3.525

Table 1 Continued

(n, a_r)	Theories	N_1	n_p	h/a = 0.05	h/a = 0.1	h/a = 0.15	h/a = 0.2	h/a = 0.3
$(4, 4.1\Delta r)$	Present	2	9	2.606	2.697	2.848	3.058	3.640
			13	2.579	2.668	2.816	3.017	3.586
			17	2.568	2.657	2.799	2.996	3.548
			19	2.565	2.653	2.793	2.988	3.528
			21	2.563	2.650	2.788	2.980	3.507
		10	9	2.606	2.697	2.848	3.058	3.640
			13	2.579	2.668	2.816	3.017	3.586
			17	2.568	2.657	2.799	2.996	3.548
			19	2.565	2.653	2.793	2.988	3.528
			21	2.563	2.650	2.788	2.980	3.507
$(4, 4.6\Delta r)$	Present	2	9	2.607	2.698	2.848	3.056	3.645
			13	2.581	2.671	2.819	3.024	3.600
			17	2.570	2.659	2.805	3.009	3.601
			19	2.567	2.655	2.801	3.007	3.585
			21	2.564	2.652	2.799	3.010	3.548
		10	9	2.607	2.698	2.848	3.056	3.645
			13	2.581	2.671	2.819	3.024	3.600
			17	2.570	2.659	2.805	3.009	3.601
			19	2.567	2.655	2.801	3.007	3.585
			21	2.564	2.652	2.799	3.010	3.548
CPT (Reddy *et al.* 1999)				2.525	2.525	2.525	2.525	NA
FSDT (Reddy *et al.* 1999)				2.554	2.639	2.781	2.979	NA
TSDT (Sahraee and Saidi 2009)				2.525	2.638	NA	2.969	3.511
FOSDT (Sahraee and Saidi 2009)				2.525	2.638	NA	2.969	3.511

Table 2 shows the SS DRK solutions of the displacement parameters at the center of the FGM circular plates with clamped edges, in which different values of thickness-to-radius ratios (h/a), material-property gradient index ($\hat{\kappa}_p$) and total number of divided layers (N_l) are considered. It can be seen that the relative errors between the displacement parameters obtained by using $N_l = 40$ and $N_l = 80$ are less than 0.6%, and the 40-layer solutions closely agree with those of FSDT, TSDT and FOSDT available in the literature. By converting the dimensionless deflection parameter to its dimensional form, the results show that the center deflection of the plate decreases when the plate becomes thicker and the material-property gradient becomes greater, which means that the gross stiffness of the plate also increase.

5.2 Sandwich FGM circular plates

In this section, we consider the static behavior of sandwich FGM circular plates with simply-supported edges and under a uniform load. The face-sheets are homogeneous ceramic layers, and

Table 2 The state space DRK and DQ solutions of the displacement components at the center of FGM circular plates with clamped edges and under a uniformly distributed load (n = 3, $a_r = 3.1\Delta r$, n_p = 21)

$\hat{\kappa}_p$	Theories	h/a = 0.05	h/a = 0.1	h/a = 0.15	h/a = 0.2
2	SS DRK (N_l = 10)	1.399	1.440	1.506	1.597
	SS DRK (N_l = 20)	1.404	1.445	1.511	1.602
	SS DRK (N_l = 40)	1.405	1.446	1.512	1.603
	SS DRK (N_l = 80)	1.405	1.447	1.513	1.603
	CPT (Reddy *et al*. 1999)	1.388	1.388	1.388	1.388
	FSDT (Reddy *et al*. 1999)	1.402	1.444	1.515	1.613
	TSDT (Sahraee and Saidi 2009)	1.388	1.443	NA	1.603
	FOSDT (Sahraee and Saidi 2009)	1.388	1.443	NA	1.603
4	SS DRK (N_l = 10)	1.276	1.312	1.372	1.455
	SS DRK (N_l = 20)	1.282	1.319	1.379	1.462
	SS DRK (N_l = 40)	1.284	1.321	1.381	1.463
	SS DRK (N_l = 80)	1.284	1.321	1.381	1.464
	CPT (Reddy *et al*. 1999)	1.269	1.269	1.269	1.269
	FSDT (Reddy *et al*. 1999)	1.282	1.320	1.384	1.473
8	SS DRK (N_l = 10)	1.172	1.207	1.264	1.343
	SS DRK (N_l = 20)	1.181	1.216	1.274	1.352
	SS DRK (N_l = 40)	1.183	1.219	1.276	1.355
	SS DRK (N_l = 80)	1.184	1.219	1.277	1.356
	CPT (Reddy *et al*. 1999)	1.169	1.169	1.169	1.169
	FSDT (Reddy *et al*. 1999)	1.181	1.217	1.278	1.362
20	SS DRK (N_l = 10)	1.076	1.110	1.166	1.243
	SS DRK (N_l = 20)	1.089	1.124	1.180	1.257
	SS DRK (N_l = 40)	1.093	1.128	1.184	1.262
	SS DRK (N_l = 80)	1.094	1.129	1.185	1.263
	CPT (Reddy *et al*. 1999)	1.080	1.080	1.080	1.080
	FSDT (Reddy *et al*. 1999)	1.092	1.126	1.184	1.265
10^5	SS DRK (N_l = 10)	1.014	1.048	1.103	1.180
	SS DRK (N_l = 20)	1.014	1.048	1.103	1.180
	SS DRK (N_l = 40)	1.014	1.048	1.103	1.180
	SS DRK (N_l = 80)	1.014	1.048	1.103	1.180
	CPT (Reddy *et al*. 1999)	1.000	1.000	1.000	1.000
	FSDT (Reddy *et al*. 1999)	1.011	1.145	1.101	1.180

the core is an FGM layer, the top and bottom planes of which are ceramic-rich, while its mid-plane is metal-rich, as shown in Fig. 3. The Poisson's ratio is assumed to remain a constant through the thickness direction of the plate, and is taken to be 0.288, while the through-thickness distributions of the Young's modulus are assumed in the following form

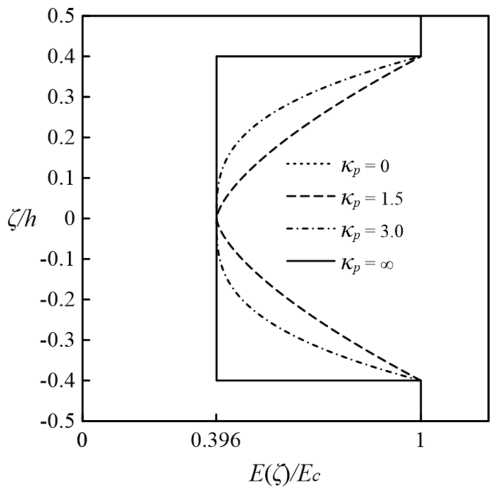

Fig. 3 The through-thickness distributions of material properties for a sandwich FGM circular plate with different values of the material-property gradient index

$$E^{(k)}(\zeta) = E_m + (E_c - E_m)\,\Gamma_c^{(k)}(\zeta), \tag{45}$$

where the superscript k denotes the k^{th}-layer, as counted from the bottom layer, and $\Gamma_c^{(k)}(\zeta)$ (k = 1 – 3) denotes the volume fractions of the ceramic material of the k^{th}-layer.

The volume fraction for each layer is given by

$$\Gamma_c^{(1)}(\zeta) = \Gamma_c^{(3)}(\zeta) = 1 \quad \text{either} \quad -0.5h \le \zeta \le -0.5h + h_f \quad \text{or} \quad 0.5h - h_f \le \zeta \le 0.5h, \tag{46a}$$

$$\Gamma_c^{(2)}(\zeta) = \left[|\zeta|/0.5h_c\right]^{\kappa_p} \qquad -0.5h_c \le \zeta \le 0.5h_c, \tag{46b}$$

where h_f and h_c denote the thickness of face sheets and core, respectively, and $2h_f + h_c = h$. The distributions of the effective Young's modulus through the thickness direction of the circular plate with $h_1 : h_2 : h_3 = 0.1h : 0.8h : 0.1h$ are shown in Fig. 3. When $\kappa_p = \infty$, the sandwich FGM circular plate will reduce to a sandwich homogeneous one, in which the face sheets are ceramic-rich layers, while the core is a metal-rich one. When $\kappa_p = 0$, the sandwich FGM circular plate will reduce to a single-layered homogeneous ceramic circular plate. In this case, the gross stiffness of this plate will increase, when the value of κ_p becomes smaller.

A set of dimensionless variables is given as follows

$$\left(\bar{u}_r,\ \bar{u}_\zeta\right) = \left(64\,D_c / q_0 a^4\right)\left(u_r,\ u_\zeta\right), \tag{47a}$$

$$\left(\bar{\sigma}_r,\ \bar{\sigma}_\theta,\ \bar{\sigma}_\zeta,\ \bar{\tau}_{r\zeta}\right) = \left(\sigma_r,\ \sigma_\theta,\ \sigma_\zeta,\ \tau_{r\zeta}\right)/q_0 . \tag{47b}$$

Fig. 4 shows the through-thickness distributions of assorted field variables induced in the sandwich FGM circular plates with different values of the material-property gradient index. It can

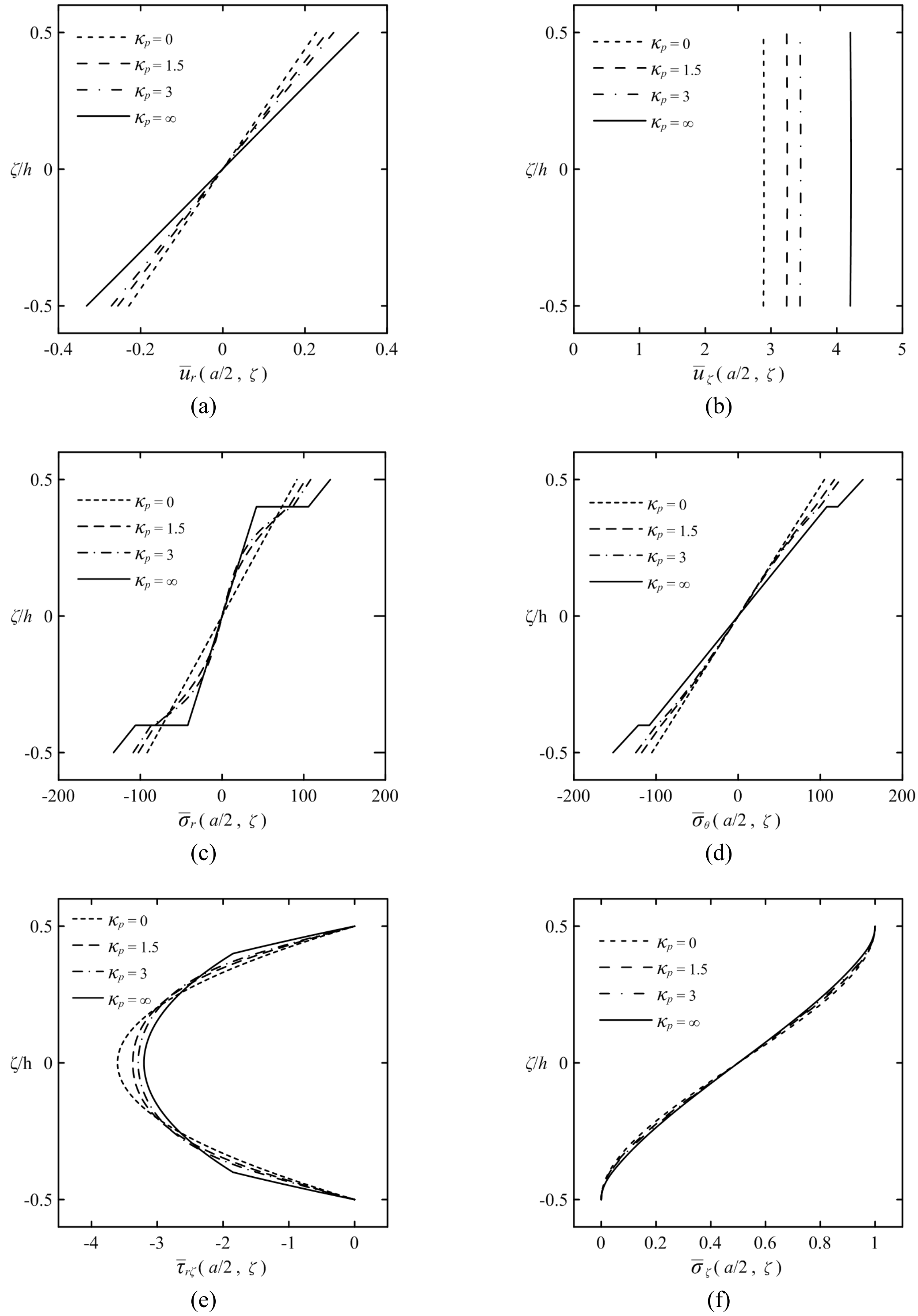

Fig. 4 The through-thickness distributions of assorted field variables induced in a simply-supported, sandwich FGM circular plate under a uniform load

be seen in Fig. 4 that for a single-layered homogeneous circular plate ($\kappa_p = 0$) these distributions of the in-plane displacement and stress components appear to be global linear functions, while they are parabolic and cubic functions for the transverse shear and normal stress components. For a sandwich homogeneous circular plate ($\kappa_p = \infty$) these distributions of the in-plane displacement and stress components appear to be layerwise linear functions, while they are layerwise parabolic and cubic functions for the transverse shear and normal stress components. The results also show that these distributions for sandwich FGM circular plates appear to be layerwise higher-order functions. These observations may provide a reference for the kinematic and kinetic assumptions when an advanced theory of sandwich FGM circular plates is to be developed.

It can be seen in Figs. 4(c) and 4(d) that the in-plane stress components induced in sandwich homogeneous circular plates ($\kappa_p = \infty$) are discontinuous when they cross the face sheet-core interfaces due to the mismatched material properties, while these are continuous for sandwich FGM ones ($\kappa_p \neq \infty$ and 0). The transverse shear stress components induced at the face sheet-core interfaces of sandwich homogeneous circular plates will be reduced for sandwich FGM ones. This might be helpful for preventing the delamination failure of sandwich FGM circular plates, which often occurs at the interfaces between adjacent layers in laminated composite structures.

6. Conclusions

On the basis of the RMVT, in this article we have developed a state space meshless method using the DRK interpolations for the 3D analysis of axisymmetric sandwich FGM circular plates with simply-supported and clamped edges. In the illustrative examples, it is shown that these state space DRK solutions converge rapidly, and are in excellent agreement with the accurate solutions available in the literature. The following guidelines were also derived with regard to the implementation of this method, such as the highest order of base functions (n) is suggested to be $n = 3$; the number of uniformly-distributed nodes (n_p) to be $n_p = 21$; and the radius of the influence zone (a_r) to be 3.1 times the spacing between the adjacent nodes (i.e., $a_r = 3.1\ \Delta r$) when $n = 3$ is used, and $a_r = 4.1\ \Delta r$ when $n = 4$ is used. It is also seen in the illustrative examples that the through-thickness distributions of the in- and out-of-surface variables of sandwich FGM circular plates appear to the layerwise linear and layerwise higher-order polynomial variations, respectively. Moreover, the transverse shear stresses induced at the interfaces between the face-sheet and core layers for sandwich FGM circular plates are reduced in comparison with those for sandwich homogeneous ones, which may prevent the delamination failure that often occurs at the interfaces between adjacent layers of sandwich homogeneous ones.

Acknowledgments

This work was supported by the Ministry of Science and Technology of the Republic of China through Grant MOST 103-2221-E-006-064-MY3.

References

Birman, V. and Byrd, L.W. (2007), "Modeling and analysis of functionally graded materials and structures", *Appl. Mech. Rev.*, **60**(5), 195-216.

Chen, W.Q. and Wang, L.Z. (2002), "Free vibrations of functionally graded piezoelectric hollow spheres

with radial polarization", *J. Sound Vib.*, **251**(1), 103-114.
Chen, W.Q., Ding, H.J. and Liang, J. (2001), "The exact elasto-electric field of a rotating piezoceramic spherical shell with a functionally graded property", *Int. J. Solids Struct.*, **38**(38-39), 7015-7027.
Chen, S.M., Wu, C.P. and Wang, Y.M. (2011), "A Hermite DRK interpolation-based collocation method for the analyses of Bernoulli-Euler beams and Kirchhoff-Lova plates", *Comput. Mech.*, **47**(4), 425-453.
Civalek, O. and Ulker, M. (2004), "Harmonic differential quadrature (HDQ) for axisymmetric bending analysis of thin isotropic circular plates", *Struct. Eng. Mech., Int. J.*, **17**(1), 1-14.
Dai, H.L., Rao, Y.N. and Dai, T. (2016), "A review of recent researches on FGM cylindrical structures under coupled physical interactions, 2000-2015", *Compos. Struct.*, **152**, 199-225.
Ebrahimi, F., Rastgoo, A. and Atai, A.A. (2009), "A theoretical analysis of smart moderately thick shear deformable annular functionally graded plate", *Eur. J. Mech A/Solids*, **28**(5), 962-973.
Hamzehkolaei, N.S., Malekzadeh, P. and Vaseghi, J. (2011), "Thermal effect on axisymmetric bending of functionally graded circular and annular plates using DQM", *Steel Compos. Struct., Int. J.*, **11**(4), 341-358.
Jha, D.K., Kant, T. and Singh, R.K. (2013), "A critical review of recent research on functionally graded plates", *Compos. Struct.*, **96**, 833-849.
Kiani, Y. and Eslami, M.R. (2013), "An exact solution for thermal buckling of annular FGM plates on an elastic medium", *Compos. Part B-Eng.*, **45**(1), 101-110.
Koizumi, M. (1997), "FGM activities in Japan", *Compos. Part B-Eng.*, **28**(1-2), 1-4.
Lal, R. and Ahlawat, N. (2015), "Axisymmetric vibrations and buckling analysis of functionally graded circular plate via differential transform method", *Eur. J. Mech. A/Solids*, **52**, 85-94.
Lei, Z.X., Liew, K.M. and Yu, J.L. (2013), "Buckling analysis of functionally graded carbon nanotube-reinforced composite plates using the element-free *kp*-Ritz method", *Compos. Struct.*, **98**, 160-168.
Li, X.Y., Ding, H.J. and Chen, W.Q. (2008), "Elasticity solutions for a transversely isotropic functionally graded circular plate subject to an axisymmetric transverse load qr^k", *Int. J. Solids Struct.*, **45**(1), 191-210.
Liang, X., Wang, Z., Wang, L. and Liu, G. (2014), "Semi-analytical solution for three-dimensional transient response of functionally graded annular plate on a two parameter viscoelastic foundation", *J. Sound Vib.*, **333**(12), 2649-2663.
Liang, X., Kou, H.L., Wang, L., Palmer, A.C., Wang, Z. and Liu, G. (2015), "Three-dimensional transient analysis of functionally graded material annular sector plate under various boundary conditions", *Compos. Struct.*, **132**, 584-596.
Lu, Y., Shi, J., Nie, G. and Zhong, Z. (2016), "An elasticity solution for transversely isotropic, functionally graded circular plates", *Mech. Adv. Mater. Struct.*, **23**(4), 451-457.
Ma, L.S. and Wang, T.J. (2004), "Relationships between axisymmetric bending and buckling solutions of FGM circular plates based on third-order plate theory and classical plate theory", *Int. J. Solids Struct.*, **41**(1), 85-101.
Müller, E., Drasar, C., Schilz, J. and Kaysser, W.A. (2003), "Functionally graded materials for sensor and energy applications", *Mater. Sci. Eng.*, **362**(1-2), 17-39.
Nie, G.J. and Zhong, Z. (2007), "Semi-analytical solution for three-dimensional vibration of functionally graded circular plates", *Comput. Methods Appl. Mech. Eng.*, **196**(49-52), 4901-4910.
Nie, G. and Zhong, Z. (2010), "Dynamic analysis of multi-directional functionally graded annular plates", *Appl. Math. Modell.*, **34**(3), 608-616.
Pan, E. (2003), "Exact solution for functionally graded anisotropic elastic composite laminates", *J. Compos. Mater.*, **37**(21), 1903-1920.
Pan, E. and Heyliger, P.R. (2003), "Exact solutions for magneto-electro-elastic laminates in cylindrical bending", *Int. J. Solids Struct.*, **40**(24), 6859-6876.
Plevako, V.P. (1971), "On the theory of elasticity of inhomogeneous media", *PMM*, **35**(5), 853-860.
Reddy, J.N. (1984a), "A simple higher-order theory for laminated composite plates", *J. Appl. Mech.*, **51**(4), 745-752.
Reddy, J.N. (1984b), *Energy and Variational Methods in Applied Mechanics*, Wiley, New York, NY, USA.
Reddy, J.N. and Berry, J. (2012), "Nonlinear theories of axisymmetric bending of functionally graded circular plates with modified couple stress", *Compos. Struct.*, **94**(12), 3664-3668.

Reddy, J.N., Wang, C.M. and Kitipornchai, S. (1999), "Axisymmetric bending of functionally graded circular and annular plates", *Eur. J. Mech. A/Solids*, **18**(2), 185-199.

Reissner, E. (1984), "On a certain mixed variational theory and a proposed application", *Int. J. Numer. Methods Eng.*, **20**(7), 1366-1368.

Reissner, E. (1986), "On a mixed variational theorem and on a shear deformable plate theory", *Int. J. Numer. Methods Eng.*, **23**(2), 193-198.

Sahraee, S. and Saidi, A.R. (2009), "Axisymmetric bending analysis of thick functionally graded circular plates using fourth-order shear deformation theory", *Eur. J. Mech. A/Solids*, **28**(5), 974-984.

Saidi, A.R., Rasouli, A. and Sahraee, S. (2009), "Axisymmetric bending and buckling analysis of thick functionally graded circular plates using unconstrained third-order shear deformation plate theory", *Compos. Struct.*, **89**(1), 110-119.

Schulz, U., Peters, M., Bach, F.W. and Tegeder, G. (2003), "Graded coating for thermal, wear and corrosion barriers", *Mater. Sci. Eng.*, **362**(1-2), 61-80

Soldatos, K.P. and Hadjigeorgiou, V.P. (1990), "Three-dimensional solution of the free vibration problem of homogeneous isotropic cylindrical shells and panels", *J. Sound Vib.*, **137**(3), 369-384.

Tornabene, F., Liverani, A. and Caligiana, G. (2012), "Laminated composite rectangular and annular plates: A GDQ solution for static analysis with a posteriori shear and normal stress recovery", *Compos. Part B-Eng.*, **43**(4), 1847-1872.

Wang, Y.M., Chen, S.M. and Wu, C.P. (2010a), "A meshless collocation method based on the differential reproducing kernel interpolation", *Comput. Mech.*, **45**(6), 585-606.

Wang, Y., Xu, R. and Ding, H. (2010b), "Three-dimensional solution of axisymmetric bending of functionally graded circular plates", *Compos. Struct.*, **92**(7), 1683-1693.

Watari, F., Yokoyama, A., Saso, F. and Kawasaki, T. (1997), "Fabrication and properties of functionally graded dental implant", *Compos. Part B-Eng.*, **28**(1-2), 5-11.

Wu, C.P. and Chang, Y.T. (2012), "A unified formulation of RMVT-based finite cylindrical layer methods for sandwich circular hollow cylinders with an embedded FGM layer", *Compos. Part B-Eng.*, **43**(8), 3318-3333.

Wu, C.P. and Jiang, R.Y. (2012), "A state space differential reproducing kernel method for the 3D analysis of FGM sandwich circular hollow cylinders with combinations of simply-supported and clamped edges", *Compos. Struct.*, **94**(11), 3401-3420.

Wu, C.P. and Jiang, R.Y. (2014), "A state space differential reproducing kernel method for the buckling analysis of carbon nanotube-reinforced composite circular hollow cylinders", *CMES-Comput. Model. Eng. Sci.*, **97**(3), 239-279.

Wu, C.P. and Jiang, R.Y. (2015a), "Three-dimensional free vibration analysis of sandwich FGM cylinders with combinations of simply-supported and clamped edges and using the multiple time scales and meshless methods", *CMC-Comput. Mater. Continua*, **46**(1), 17-56.

Wu, C.P. and Jiang, R.Y. (2015b), "An asymptotic meshless method for sandwich functionally graded circular hollow cylinders with various boundary conditions", *J. Sandw. Struct. Mater.*, **17**, 469-510.

Wu, C.P. and Li, H.Y. (2010), "The RMVT- and PVD-based finite layer methods for the three-dimensional analysis of multilayered composite and FGM plates", *Compos. Struct.*, **92**(10), 2476-2496.

Wu, C.P. and Li, H.Y. (2013a), "An RMVT-based finite rectangular prism method for the 3D analysis of sandwich FGM plates with various boundary conditions", *CMC-Comput. Mater. Continua*, **34**(1), 27-62.

Wu, C.P. and Li, H.Y. (2013b), "RMVT-based finite cylindrical prism methods for multilayered functionally graded circular hollow cylinders with various boundary conditions", *Compos. Struct.*, **100**, 592-608.

Wu, C.P. and Li, W.C. (2016), "Quasi-3D stability and vibration analyses of sandwich piezoelectric plates with an embedded CNT-reinforced composite core", *Int. J. Struct. Stab. Dyn.*, **16**(2), 1450097.

Wu, C.P. and Liu, K.Y. (2007), "A state space approach for the analysis of doubly curved functionally graded elastic and piezoelectric shells", *CMC-Comput. Mater. Continua*, **6**(3), 177-199.

Wu, C.P. and Liu, Y.C. (2016), "A review of semi-analytical numerical methods for laminated composite and multilayered functionally graded elastic/piezoelectric plates and shells", *Compos. Struct.*, **147**, 1-15.

Wu, C.P. and Tsai, T.C. (2012), "Exact solutions of functionally graded piezoelectric material sandwich cylinders by a modified Pagano method", *Appl. Math. Modell.*, **36**(5), 1910-1930.
Zhu, P., Lei, Z.X. and Liew, K.M. (2012), "Static and free vibration analyses of carbon nanotube-reinforced composite plates using finite element method with first order shear deformation plate theory", *Compos. Struct.*, **94**(4), 1450-1460.

CC